Computational Study on the Photolysis of BrHgONO and the Reactions of BrHgO• with CH_4, C_2H_6, NO, and NO_2: Implications for Formation of Hg(II) Compounds in the Atmosphere

Khoa T. Lam, Curtis J. Wilhelmsen, Abraham C. Schwid, Yuge Jiao, Theodore S. Dibble*

Department of Chemistry, State University of New York-College of Environmental Science and Forestry, 1 Forestry Dr., Syracuse, NY, 13210, United States

ABSTRACT

Global models suggest BrHgONO to be the major Hg(II) species initially formed in atmospheric oxidation of Hg(0) in most of the atmosphere, but its atmospheric fate has not been previously investigated. In the present work, we use quantum chemistry to predict that BrHgONO photolysis to produce the thermally stable radical BrHgO•. Subsequently, BrHgO• may react with NO_2 to form thermally stable $BrHgONO_2$, or with NO to reform BrHgONO. Additionally, BrHgO• abstracts hydrogen atoms from CH_4 and C_2H_6 with higher rate constants than does •OH, producing a stable BrHgOH molecule. Because BrHgO• can abstract hydrogen atoms from sp^3-hybridized carbons on many organic compounds, we expect production of BrHgOH to dominate globally, although formation of BrHgONO and $BrHgONO_2$ may compete in urban regions. In the absence of experimental data on the kinetics and fate of BrHgONO and BrHgO•, we aim to guide modelers and scientists in their search for Hg(II) compounds in the atmosphere.

INTRODUCTION

Mercury (Hg)—a neurotoxic pollutant which damages both human health and ecosystems, globally—exists in the atmosphere predominantly in its elemental form (Hg(0), GEM).[1] Only a modest fraction of atmospheric mercury exists in the form of gaseous oxidized mercury compounds (GOM, mostly Hg(II)), because they readily undergo dry and wet deposition to soil and water.[2,3] Upon entering ecosystems, these compounds can be transformed into organomercury compounds which subsequently bioaccumulate up the food chain and may ultimately be consumed by humans. There exists only operational definition for GOM compounds, and their chemical identities are not known. Laboratory experiments on gas-phase mercury chemistry are challenging, mainly due to the tendency for surfaces to catalyze reactions and trap relatively nonvolatile reaction products. As a result, the kinetics and mechanism of mercury oxidation in the gaseous atmosphere remain highly uncertain. This ignorance has created substantial uncertainties in global models of the fate and transport of mercury.[4]

Atomic bromine (Br•) has been strongly suggested by modeling and field studies[5,6] to initiate GEM oxidation in the marine boundary layer and in atmospheric mercury depletion events in the Polar Regions. Some modeling efforts[5,7,8] further argue that the oxidation initiated by Br• alone can account for GEM oxidation, globally. Additionally, both experiments[9] and computations[10,11] support the kinetics and thermodynamics of the initiating step:

$$\mathrm{Hg} + \mathrm{Br}\bullet + \mathrm{M} \leftrightarrows \mathrm{BrHg}\bullet + \mathrm{M} \quad (1)$$

where M is another molecule in the gas phase. Despite its relatively weak bond (15.5 kcal mol^{-1}),[12] BrHg• can react with other radical species in the atmosphere before dissociating. By contrast, no experimental evidence exists on the subsequent chemistry of BrHg•, however. Until recently, only two reactions have been included in atmospheric models: the barrierless reactions with Br• and •OH to form the stable gas-phase compounds $HgBr_2$ and BrHgOH.[10]

Dibble et al.[13] argued that the barrierless additions of several radicals to BrHg•:

$$\mathrm{BrHg}\bullet + \mathrm{NO_2} + \mathrm{M} \leftrightarrows \textit{syn}\text{-BrHgONO} + \mathrm{M} \quad (2)$$

$$\mathrm{BrHg}\bullet + \mathrm{HO_2} + \mathrm{M} \leftrightarrows \textit{syn}\text{-BrHgOOH} + \mathrm{M} \quad (3)$$

are much more relevant for BrHg• in the global atmosphere (than reaction with •OH and Br•), due to their much higher concentrations of NO_2 and HO_2. Coburn et al.[14] used fieldwork and modeling to determine that inclusion of these reactions enormously increased the rate of GEM oxidation in the troposphere. Subsequently, Dibble and Jiao[15] computed and confirmed their high rate constants as a function of temperature and pressure. More recently, using these rate constants, Ye et al.[16] demonstrated improvements in the performance of the CMAQ regional model, reproducing for the first time the distinct pattern of a GOM daytime maximum at their marine site. Horowitz et al.[7] incorporated these rate constants in the GEOS-CHEM global model, and improved previous predictions of latitudinal gradients of GOM deposition fluxes. They also confirmed that NO_2 and HO_2 dominate the oxidation of BrHg• globally. Computations by Dibble and Schwid ruled out reactions with most volatile organic compounds (VOCs) due to unfavorable thermodynamics. All in all, these results suggest *syn*-BrHgONO (and BrHgOOH) to be the major GOM species produced by GEM oxidation from Br•.

Saiz-Lopez et al.[17] in a recent work computed ultraviolet absorption cross-section spectra for various postulated GOM species including *syn*-BrHgONO (and BrHgOOH) using the CASSCF/MS-CASPT2/SO-RASSI level of theory. They demonstrated that *syn*-BrHgONO can undergo photolysis at fast timescales in the troposphere (annually and globally averaged lifetime of ~20 minutes assuming a quantum yield of unity). In their atmospheric modeling, BrHgONO photolysis was assumed, based on photodissociation pathways of $HgBr_2$,[18,19] to produce BrHg• or to Hg(0). In the present work, we use computational chemistry to demonstrate that the photolysis of *syn*-BrHgONO occurs via a different route:

$$\textit{syn}\text{-BrHgONO} + h\nu \rightarrow \text{BrHgO}\bullet + \text{NO} \quad (4)$$

and that this pathway occurs rapidly in lowermost atmosphere (~30 minutes under clear sky conditions). The fast timescale also suggests BrHgO• to be an important intermediate in GEM oxidation. No experimental data exists on BrHgO•, but Balabanov and Peterson[20] used CCSD(T) calculations to determine that it possesses strong Br–Hg (60 kcal mol^{-1}) and Hg–O bonds (70 kcal mol^{-1}). We thereby infer that BrHgO• decomposes slowly in the gas phase, so that it exists long enough to react further with atmospheric trace gases.

The present work explores two types of reactions of BrHgO•: hydrogen abstraction from two model alkanes (CH_4 and C_2H_6) and addition to NO and NO_2:

$$\text{BrHgO}\bullet + CH_4 \rightarrow \text{BrHgOH} + \bullet CH_3 \quad (5)$$

$$\text{BrHgO}\bullet + C_2H_6 \rightarrow \text{BrHgOH} + \bullet C_2H_5 \quad (6)$$

$$\text{BrHgO}\bullet + \text{NO} \rightarrow \textit{syn}\text{-BrHgONO} \quad (7)$$

$$\text{BrHgO}\bullet + NO_2 \rightarrow \text{BrHgONO}_2 \quad (8)$$

In particular, we report the potential energy profiles for all four reactions and the rate constants for the reactions with CH_4 and C_2H_6. Additionally, we assess the likely fates of BrHgOH and $BrHgONO_2$ in the atmosphere, and provide directions for future research on the chemistry of BrHgO•.

METHODS

The standard Dunning correlation consistent basis sets aug-cc-pVXZ (X = D, T, Q)[21,22] were used for hydrogen, carbon, oxygen, and nitrogen atoms. The small-core Stuttgart/Cologne scalar relativistic pseudopotentials for Br (10 electrons) and Hg (60 electrons)[23,24] were used in conjunction with the corresponding aug-cc- pVXZ (X = D, T, Q) basis sets for the electrons treated explicitly. We refer to this combination of basis set as AVXZ (X = D, T, Q) hereafter. Although basis sets with pseudopotentials may not be sufficient in describing systems with strong spin-orbit couplings,[25] no bonds to the Br or Hg are broken in the ground- or excited-state chemistry considered here. As a result, we expect spin-orbit contributions to the relative energies to be small.

Time-dependent density functional theory (TD-DFT)[26] was used as a starting point to characterize excited states of *syn*-BrHgONO using Gaussian 09 revision D.01.[27] Results were refined using equations of motion (EOM) variant[28] of the coupled cluster singles and doubles (CCSD) method[29] using CFOUR.[30] Vertical excitation energies and oscillator strengths for the four lowest-lying excited states of A' and A" symmetry were at both PBE1PBE (PBE0)/AVTZ[31] and CCSD/AVTZ from the

ground state geometries computed at the same level of theory. The structure and vibrational frequencies of the lowest-lying singlet excited state (S_1) were computed at TD-PBE0/AVTZ and EOM-CCSD/AVTZ.

Studies of the thermal reactions of BrHgO• were performed using Gaussian 09 revision D.01. Geometry optimizations were performed on all stationary points (reactants, products, and saddle points) at M06-2X/AVTZ.[32] Harmonic frequencies were computed using analytical second derivatives to verify local minima (all real frequencies) or transition states (one imaginary frequency). Unscaled harmonic vibrational frequencies were used to compute zero-point vibrational energies (ZPE). The optimizations at the M06-2X level of theory used a pruned "ultrafine" grid of 99 radial shells with 590 angular points per shell. Calculations for open-shell species were performed with the spin unrestricted formalism. Energies of all stationary points were refined using CCSD with perturbative triples (CCSD(T)) method[33] in conjunction with the AVTZ basis set. CCSD(T) calculations were performed with the frozen core approximation, in which only the molecular orbitals of Hg (5d6s), Br (4s4p), C (2s2p), O (2s2p), N (2s2p), and H (1s) electrons were correlated; for Hg and Br, these definitions of the frozen core are not the defaults in Gaussian 09. Unless otherwise specified, all relative energies reported in the present work for reactions of BrHgO• were computed at CCSD(T)//M06-2X/AVTZ.

Relative energies reported are at 0 K and corrected with ZPE, and therefore are equivalent to enthalpy changes at 0 K. Rate constants, $k^{CTST}(T)$, for reactions 5 and 6 were computed using canonical transition state theory (CTST), given by:

$$k^{CTST}(T) = \kappa(T)(k_B T/h) \exp(-\Delta G^{\dagger}(T)/RT) \quad (9)$$

where k_B, h, and R are Boltzmann's constant, Planck's constant, and the ideal gas constant, respectively; $\Delta G^{\dagger}(T)$ is the molar Gibbs free energy of activation; and $\kappa(T)$ is the tunneling coefficient. Changes in Gibbs free energies were computed using the rigid rotor and harmonic oscillator approximations. Rate constants were refined using variational transition state theory (VTST), in which canonical rate constants were calculated for multiple points along the minimum energy path (MEP). The minimum rate constant found along the MEP corresponds to the variational rate constant, $k^{VTST}(T)$. As rotational symmetry numbers were the default in the Gibbs free energy calculations and none of the reactants or saddle points possess optical isomers, equation 9 does not need a separate term for reaction path degeneracy. Tunneling was calculated using the asymmetric Eckart potential for reaction 5 only. The neglect of tunneling in reaction 6 is justified in the Results and Discussion. All rate constants were reported in the temperature range of 200 K ≤ T ≤ 2000 K, which covers both the lowest temperature typical of the troposphere and high temperatures relevant to mercury oxidation in coal combustion.

The kinetics of the additions of BrHgO• to NO and NO_2 was not computed in the present work. Treating the strong electron correlation of these bond-forming processes would require a multireference approach coupled with a large basis set. Given the absence of experimental data with which to evaluate the accuracy of these computationally demanding calculations, computed rate constants might not be more reliable than educated guesses; these guesses are provided in the Results and Discussion.

RESULTS AND DISCUSSION

BrHgONO excited states. EOM-CCSD/AVTZ values of the vertical excitation energies of the four lowest singlet states of syn-BrHgONO are listed in **Table 1**, along with the adiabatic excitation energy. For comparison purposes, **Table 1** includes the analogous results for the lowest energy (*trans*) isomer of HONO. The Supporting Information lists the same information at PBE0/AVTZ. From **Table 1**, one can see that BrHgONO, similar to HONO, possesses a first singlet excited (S_1) state of A" symmetry which absorbs at wavelengths that reach the lowermost atmosphere ($\lambda > 300$ nm, corresponding to energies less than ~4.1 eV). For HONO, the computed vertical excitation energy of this $n\rightarrow\pi^*$ transition of 3.57 eV (347 nm) at EOM-CCSD is in good agreement with experiment, although precise comparisons are difficult due to the strong vibrational structure of the spectrum.[34,35] For BrHgONO, the corresponding state possesses a vertical excitation energy of 3.95 eV (314 nm). The computed adiabatic excitation energies of BrHgONO and HONO are 3.49 eV and 3.36 eV, respectively.

Table 1. EOM-CCSD/AVTZ vertical excitation energies (VEE, in eV, with adiabatic values in parentheses for the S_1 state only) and oscillator strengths, *f*, for the lowest energy conformer of BrHgONO and HONO.

State	*syn*-BrHgONO		*trans*-HONO	
	VEE	*f*	VEE	*f*
1 A"	3.95 (3.49)	8.6×10^{-4}	3.57 (3.36)	1.0×10^{-3}
2 A'	5.20	1.0×10^{-2}	6.95	4.0×10^{-2}
2 A"	5.22	1.3×10^{-2}	7.63	5.4×10^{-4}
2 A'	5.63	4.7×10^{-2}	7.64	5.0×10^{-2}

Computations and experiments indicate that the S_1 state of HONO dissociates via a modest- to no-barrier process at ultrafast timescales.[36–38] Using TD-DFT, we find two transition states for BrHgO–NO bond fission, one each of *syn* and *anti* conformation with respect to the HgONO dihedral angle. Their structures, together with that of the ground and S_1 state of *syn*-BrHgONO, are depicted in **Figure 1**. Computed barrier heights (without ZPE) are 1.2 kcal mol^{-1} (*anti*) and 2.7 kcal mol^{-1} (*syn*) at TD-PBE0/AVTZ. In the present work, barrier heights refer to the energy threshold to reaction without ZPE, whereas critical energies refer to the ZPE-included value. Using EOM-CCSD/AVTZ, a rigid scan of the BrHgO–NO coordinate suggests the near-absence of a barrier to dissociation. By comparison, CASPT2 calculations on HONO reported in the literature showed either no barrier (at CISD+Q) or a minuscule barrier (0.15 kcal mol^{-1} at CASPT2).[37] Similarly low barriers have been reported for CH_3ONO dissociation.[39,40] Our TD-DFT calculations showed a barrier of 3.7 kcal mol^{-1} for HONO and 1.2 kcal mol^{-1} for *syn*-BrHgONO. All these lines of evidence point to the conclusion that photoexcitation of BrHgONO to the S_1 state results in dissociation with a quantum yield of unity to break the BrHgO–NO bond, analogous to the photodissociation of HONO.

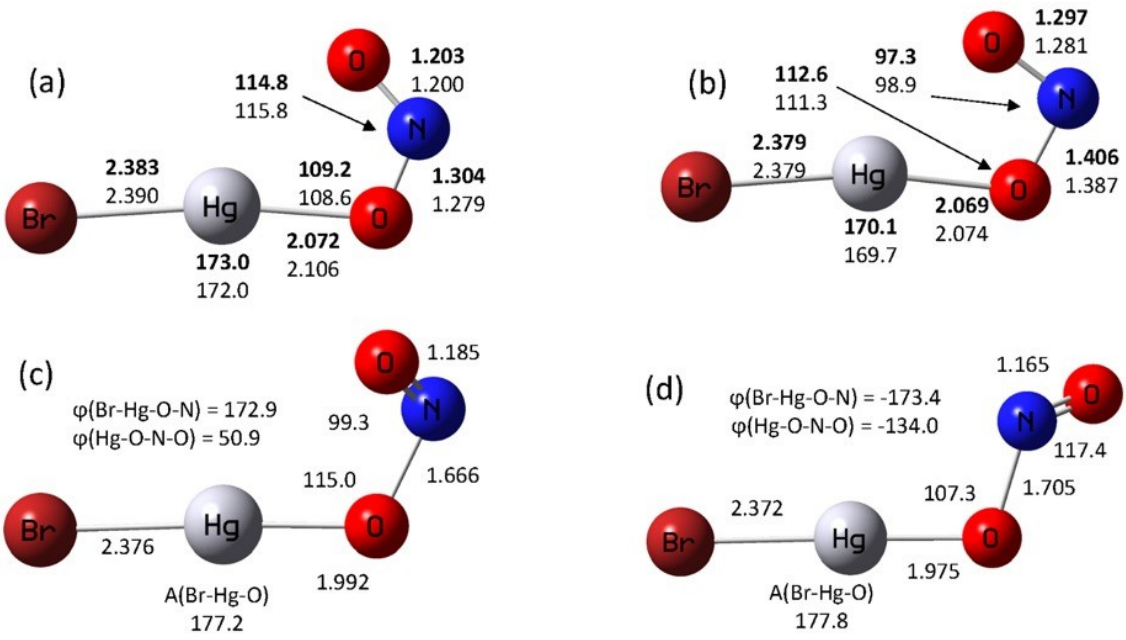

Figure 1. Structures of the (a) ground and (b) first singlet excited state (S_1) of BrHgONO, and structures of the transition states for dissociation of the (c) *syn* and (d) *anti* conformers of the S_1 state. Distances are listed in Å and angles in degrees. Bold font indicates structural data at CCSD or EOM-CCSD results while normal font indicates PBE0 or TD-PBE0 results. All structures were computed using the AVTZ basis set.

Although it would be interesting to compute the structure of the absorption spectrum of BrHgONO in detail, it is clear that experiment and theory have yet to provide good agreement for the width of the vibrational structure in HONO.[37,41] In addition, the heavy atoms present in BrHgONO would necessitate treatment of spin-forbidden transitions to the first triplet excited state. At this time, we choose a more heuristic approach: we approximate the spectrum of BrHgONO as the spectrum of HONO blue-shifted by the 33-nm difference in the vertical excitation energies of the two molecules. Given the similarity of the absorption spectrum of HONO with that of FNO and organic nitrites (RONO), we feel this approximation is quite reasonable. HONO has a photolysis lifetime of about 13 minutes under clear sky conditions at a solar zenith angle of 40 degrees. Were its spectrum blue-shifted by 33 nm, its photolysis lifetime under the same conditions would be roughly 22 minutes. The oscillator strength for HONO is about 20% larger than that for BrHgONO. Accounting these two factors, the photolysis lifetime of BrHgONO under these conditions may be crudely estimated as 30 minutes. A recent paper by Saiz-Lopez et al.[17] suggested a very similar photolysis lifetime for BrHgONO, but did not provide peak assignments. For excited state determinations, spin-orbit effects may be introduced due to multi-state mixing, however, the $S_0 \rightarrow S_1$ transition of BrHgONO corresponds to a $n \rightarrow \pi^*$ transition of the N=O group,[42] so the effect of spin-orbit coupling on the transition energy should be small. Note, however, that our photolysis lifetime neglects any intensity due to transitions from the ground to the first triplet state. Given that almost all non-radical trace gases in the atmosphere have lifetimes of hours to days with respect to reactions other than photolysis,[43] we expect that photolysis dominates the fate of BrHgONO in the atmosphere. This

conclusion is insensitive to the uncertainties in the approach used here to compute the photolysis lifetime of BrHgONO.

BrHgO• + CH_4 reaction. To verify the accuracy of our computational approach in the absence of experimental data on BrHgO• kinetics, we examined the analogous reaction •OH + CH_4 → HOH + •CH_3. Our goal was to select a method for geometry optimizations and frequencies that obtains a good barrier height and reaction enthalpy. We considered M06-2X and PBE0 due to their excellent performance for organomercury compounds[44] and in our previous research on inorganic mercury compounds.[45] Additionally, we tested the higher level CCSD/AVTZ approach. **Figure 2** compares relative energies for the •OH + CH_4 system computed with few theoretical methods to various highly accurate results by Ellingson et al.[46] M06-2X performed much better than PBE0 and CCSD with regard to both barrier height and reaction enthalpy at 0 K. Consequently, we performed geometry optimizations of all species at M06-2X/AVTZ and refined their energies at CCSD(T)/AVTZ.

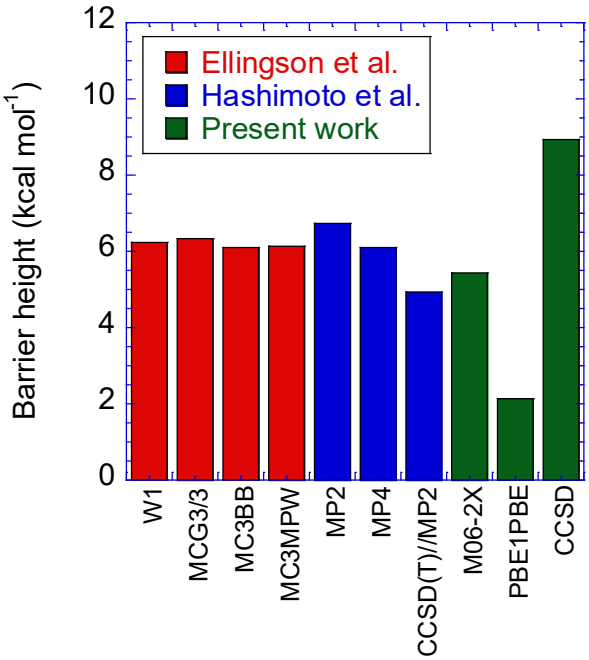

Figure 2. Barrier heights (without ZPE) for the •OH + CH_4 reaction computed with few theoretical methods (green) using the AVTZ basis set compared to benchmark results from Ellingson et al.[46] (red). Values reported by Hashimoto et al.[47] (blue, using the AVTZ basis set) display the benefit of refining energies using the CCSD(T) level of theory.

Figure 3 displays the potential energy profile and **Table 2** lists the relative energies of stationary points for the BrHgO• + CH_4 reaction. BrHgO• abstracts a hydrogen atom from CH_4 by overcoming a modest energy barrier of 2.6 kcal mol^{-1} at CCSD(T)//M06-2X/AVTZ. **Figure 4** displays the structures of reactants, products, and saddle point of the BrHgO• + CH_4 reaction and **Table 3** lists the vibrational frequencies and IR intensities of BrHgOH at M06-2X/AVTZ. As depicted in **Figure 4**, upon going from BrHgO• to the closed-shell BrHgOH, the BrHgO angle deviates from linearity by 3°, and the lengths of Br–Hg and Hg–O bonds only change by ~0.001 Å. At M06-2X/AVTZ, the BrHgO–H is only 0.001 Å longer than that of HO–H. Notably, the computed harmonic stretching

frequency of 249 cm^{-1} for the Br–Hg bond agrees with the experimental frequency of 238 cm^{-1} reported by Clarke et al.[48]

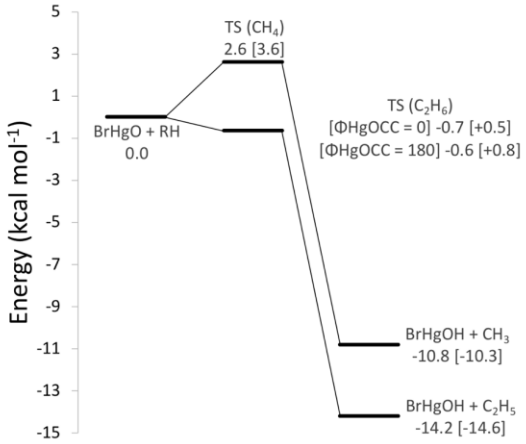

Figure 3. ZPE-corrected relative energies for the BrHgO• + CH_4 and BrHgO• + C_2H_6 reactions at CCSD(T)//M06-2X/AVTZ. Energies are listed for both conformers of the saddle point for the BrHgO• + C_2H_6 reaction. The values in brackets are energies at M06-2X/AVTZ.

Table 2. Reaction enthalpies at 0 K (ΔH_r, in kcal mol^{-1}) and critical energies (E_0, in kcal mol^{-1}) for the BrHgO• + CH_4 and BrHgO• + C_2H_6 reactions using the AVTZ basis set. The two conformers of the saddle point for the BrHgO• + C_2H_6 reaction possess Φ[HgOCC] of 0° and 180°. CCSD(T) energies are obtained at the M06-2X/AVTZ geometries.

	ΔH_r (0 K)		E_0	
	M06-2X	CCSD(T)	M06-2X	CCSD(T)
BrHgO• + CH_4 → BrHgOH + •CH_3	-10.3	-10.8	3.6	2.6
BrHgO• + C_2H_6 → BrHgOH + •C_2H_5	-14.5	-14.2	+0.5 (Φ = 0°) +0.8 (Φ = 180°)	-0.6 (Φ = 0°) -0.7 (Φ = 180°)

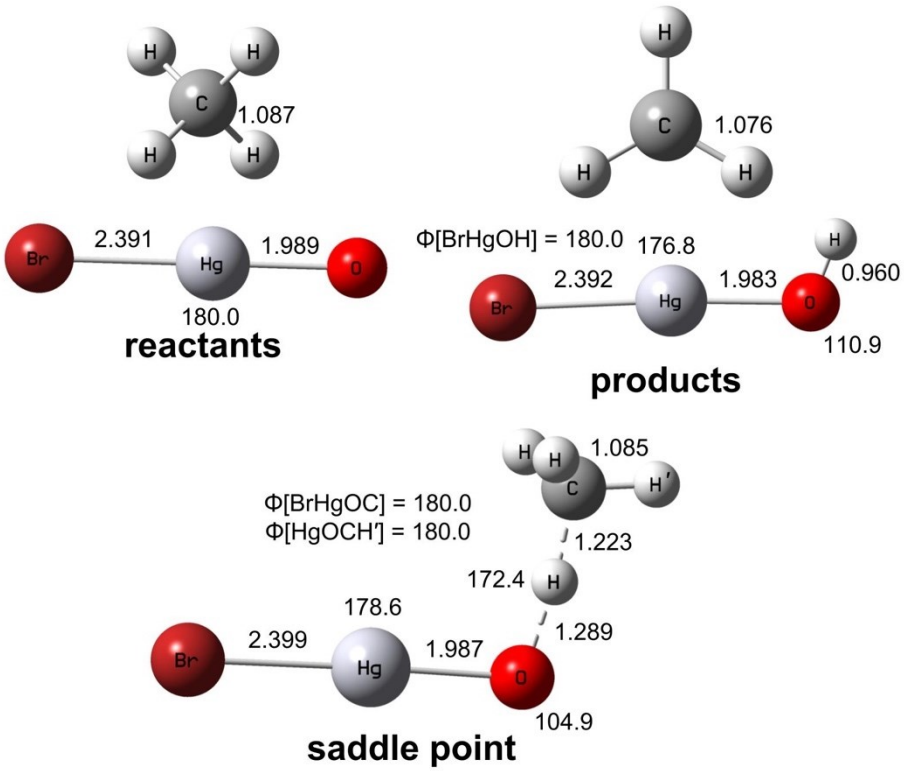

Figure 4. Reactants, products, and saddle point for the BrHgO• + CH_4 reaction at M06-2X/AVTZ. Distances are listed in Å and angles in degrees.

Table 3. Vibrational modes, symmetries, harmonic frequencies ($\tilde{\nu}$, in cm^{-1}), and integrated absorption intensities (S, in km mol^{-1}) of BrHgOH at M06-2X/AVTZ.

Mode description	Symmetry	$\tilde{\nu}$	S
BrHgO in-plane bend	A'	122	6.28
BrHgO out-of-plane bend	A"	124	0.17
BrHg stretch	A'	249	9.72
HgO stretch	A'	595	90.0
HgOH in-plane bend	A'	907	44.4
OH stretch	A'	3890	88.5

To determine the BrHgO–H bond dissociation energy, we considered these isodesmic reactions:

$$BrHgO\bullet + H_2O \rightarrow BrHgOH + \bullet OH \quad (10)$$

$$BrHgO\bullet + CH_3OH \rightarrow BrHgOH + CH_3O\bullet \quad (11)$$

Averaged over these two reactions, the BrHgO–H bond possesses a dissociation energy of 114.5 ± 0.3 kcal mol^{-1} (at CCSD(T)//M06-2X/AVTZ, 0 K), only 2.8 kcal mol^{-1} lower than that of HO–H, but higher by a full 10.3 kcal mol^{-1} than that of CH_3O–H. The Supporting Information provides the computed energies and literature data on enthalpies of formation used to calculate the bond dissociation energy.

Figure 5 displays the basis set effect on the CCSD(T) barrier heights for the •OH + CH_4 and BrHgO• + CH_4 reactions. In both systems, increasing the basis set from AVDZ to AVTZ lowered the CCSD(T) barrier by less than 0.1 kcal mol^{-1}. In hydrogen abstraction by •OH, extending the basis set from AVTZ to AVQZ lowered the barrier by only 0.08 kcal mol^{-1}. The minimal change in barrier upon increasing from AVTZ to AVQZ in the •OH system, along with the similar trends of the BrHgO• and •OH systems, suggest that little benefit could be gained from computing the CCSD(T)/AVQZ energy of the saddle point for the BrHgO• + CH_4 reaction. The CCSD(T) rate constants computed by Hashimoto et al.[47] have, however, overestimated the experimental result by one order of magnitude at 298 K, consistent with their barrier height being 1.3 kcal mol^{-1} lower than the benchmark values reported by Ellingson et al.[46] (see **Figure 2**). Consequently, one may reasonably expect our results for the BrHgO• + CH_4 reaction to underestimate the barrier height by a similar amount, leading to an overestimate of rate constants.

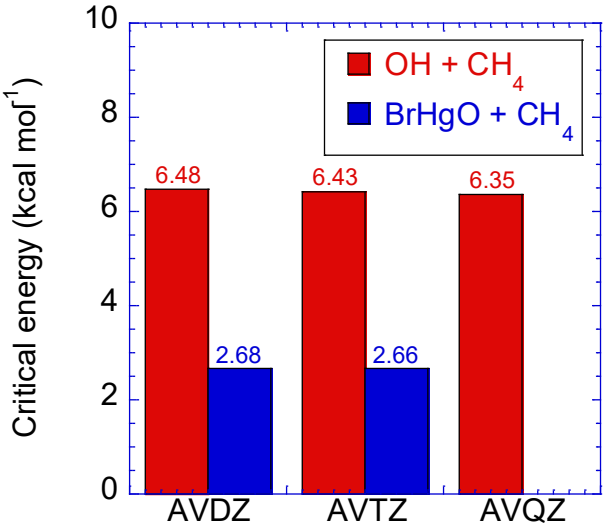

Figure 5. Critical energies (ZPE-corrected, in kcal mol^{-1}) for the •OH + CH_4 reaction adapted from Hashimoto et al.[47] (red, at CCSD(T)//MP2) compared to those of the BrHgO• + CH_4 reactions (blue, at CCSD(T)//M06-2X).

Figure 6 displays the rate constants as a function of temperature for the BrHgO• + CH_4 reaction and **Table 4** lists the canonical rate constants along with corrections for the variational effect and Eckart tunneling correction. At 298 K, BrHgO• abstracts a hydrogen from CH_4 at a rate constant of 2.3×10^{-13} molecules cm^{-3} s^{-1}, approximately 30 times faster than •OH + CH_4. The variational effect significantly lowers the rate constants; k^{VTST}/k^{CTST} ranges from 0.63 to 0.89 at 200 K and 2000 K, respectively. The positions of the variational transition states, s^{VTST}, were found on the reactant side at all temperatures, varying from -0.10 to -0.04 a_0.

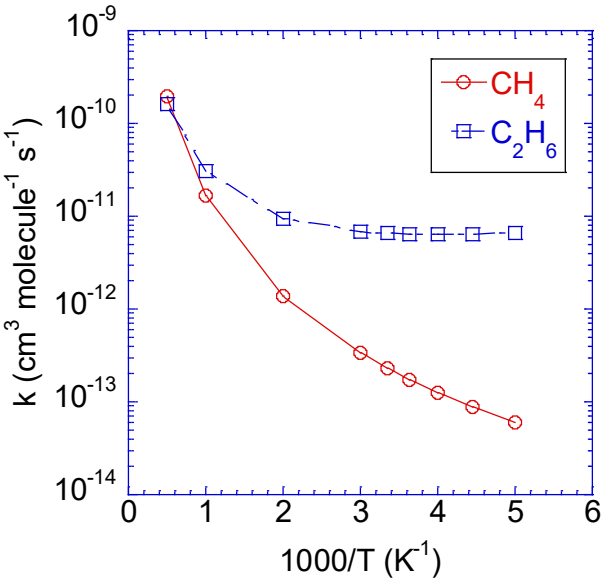

Figure 6. Variational rate constants (k^{VTST}, in cm^3 $molecule^{-1}$ s^{-1}) for the BrHgO• + CH_4 (red circle) and BrHgO• + C_2H_6 (blue square) reactions at CCSD(T)//M06-2X/AVTZ. Rate constants for the BrHgO• + CH_4 reaction include Eckart tunneling correction, whereas those for the BrHgO• + C_2H_6 do not.

Table 4. Temperature dependence of the variational transition state position (s^{VTST}, in a_0), canonical rate constants (k^{CTST}, in cm^3 $molecule^{-1}$ s^{-1}), variational (k^{VTST}/k^{CTST}) and Eckart tunneling (κ^{Eckart}) corrections, and effective rate constants ($k^{Eckart\ +\ VTST}$) for the BrHgO• + CH_4 reaction at CCSD(T)//M06-2X/AVTZ. Values in parentheses are exponents of 10.

T (K)	s^{VTST}	k^{CTST}	k^{VTST}/k^{CTST}	κ^{Eckart}	$k^{Eckart\ +\ VTST}$
200	-0.1048	6.3 (-15)	0.63	14.71	5.9 (-14)
225	-0.0943	1.4 (-15)	0.69	9.03	8.8 (-14)
250	-0.0838	2.7 (-14)	0.73	6.26	1.2 (-13)
275	-0.0733	4.8 (-14)	0.76	4.73	1.7 (-13)
298	-0.0733	7.5 (-14)	0.78	3.86	2.3 (-13)
333	-0.0629	1.3 (-13)	0.81	3.04	3.3 (-13)
500	-0.0524	9.3 (-13)	0.86	1.72	1.3 (-12)
1000	-0.0419	1.6 (-11)	0.89	1.17	1.6 (-11)
2000	-0.0419	2.0 (-10)	0.89	1.05	1.9 (-10)

Tunneling effect significantly increases BrHgO• + CH_4 canonical rate constants at low temperatures (by factors of 15 and 3 at 200 K and 333 K, respectively). The extent of Eckart tunneling varies largely on the magnitude of the imaginary frequency at the saddle point. For the •OH + CH_4 system, the imaginary frequency magnitude depends largely on the level of theory (982*i* and 1422*i* cm^{-1} at M06-2X/AVTZ and UCCSD(T)-F12a/AVTZ[49], respectively), whereas that for the BrHgO• system remains reasonably method-independent (~1300*i* cm^{-1}). It should be noted, however, that Eckart tunneling does not suffice compared to zero-curvature (ZCT)[47,50] and small-curvature tunneling (SCT)

for the •OH + CH_4 reaction.[46,49,50] As a result, we do not expect Eckart tunneling to be sufficient in treating tunneling effect in the BrHgO• + CH_4 reaction.

BrHgO• + C_2H_6 reaction. Figure 3 displays the potential energy profile and **Table 2** lists the relative energies of stationary points for the BrHgO• + C_2H_6 reaction. BrHgO• may abstract a hydrogen atom from C_2H_6 to form BrHgOH via two saddle points of C_s symmetry. **Figure 7** depicts the structure of these saddle points along with that of C_2H_6 and C_2H_5•. One saddle point possesses a folded geometry (Φ[HgOCC] = 0°), whereas the other displays an extended geometry (Φ[HgOCC] = 180°). CCSD(T) barrier heights (without ZPE) for the saddle points are positive, as do those computed at the M06-2X level of theory. Their CCSD(T) critical energies (ZPE-included) are negative, however. Our kinetics calculations used the negative CCSD(T) barrier heights and neglected tunneling. Because the two saddle points lead to the same products, their variational rate constants were added to give an effective rate constant.

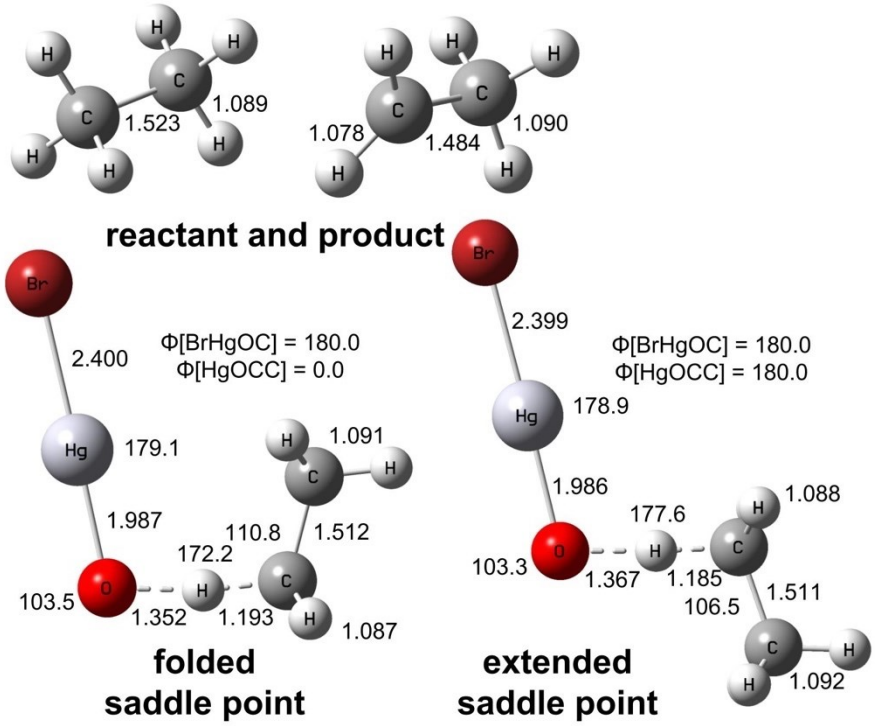

Figure 7. Reactants, products, and both conformers of the saddle point for the BrHgO• + C_2H_6 reaction at M06-2X/AVTZ. Distances are listed in Å and angles in degrees.

Figure 6 displays the rate constants as a function of temperature for the BrHgO• + C_2H_6 reaction and **Table 5** lists the rate constants along with the contributions and variational effects of both saddle points. The rate constant becomes nearly temperature independent at lower temperatures (200 to 333 K), but exhibits positive curvature at higher temperatures. Rate constants for BrHgO• + C_2H_6 are significantly higher than those for BrHgO• + CH_4 at almost all temperatures. Curiously, at 2000 K the computed rate constant for hydrogen abstraction from CH_4 falsely exceeds that from C_2H_6 by ~15%. Despite the unphysical result at 2000 K (likely due to the breakdown of the harmonic oscillator

approximation), we are confident that rate constants computed at lower temperatures (T < 1000 K) are reasonable.

Table 5. Rate constants (k^{VTST}, in cm^3 $molecule^{-1}$ s^{-1}) for the BrHgO• + C_2H_6 reaction, along with the position of the variational transition state (s^{VTST}, in a_0) and variational corrections for each conformer of the saddle point at CCSD(T)//M06-2X/AVTZ. Values in parentheses are exponents of 10.

T (K)	Φ[HgOCC] = 0°			Φ[HgOCC] = 180°			k^{VTST}
	s^{VTST}	k^{CTST}	k^{VTST}/k^{CTST}	s^{VTST}	k^{CTST}	k^{VTST}/k^{CTST}	
200	-0.0111	2.0 (-12)	0.99	-0.0242	4.7 (-12)	0.94	6.5 (-12)
225	0.0000	1.9 (-12)	1.00	-0.0121	4.6 (-12)	0.98	6.4 (-12)
250	0.0223	1.8 (-12)	0.98	-0.0121	4.6 (-12)	1.00	6.4 (-12)
275	0.0335	1.8 (-12)	0.96	0.0000	4.7 (-12)	1.00	6.4 (-12)
298	0.0335	1.8 (-12)	0.94	0.0121	4.9 (-12)	0.99	6.5 (-12)
333	0.0447	1.9 (-12)	0.91	0.0242	5.2 (-12)	0.97	6.8 (-12)
500	0.0671	2.7 (-12)	0.81	0.0727	8.2 (-12)	0.87	9.3 (-12)
1000	0.0895	9.4 (-12)	0.71	0.1091	3.1 (-11)	0.74	3.0 (-11)
2000	0.1007	5.3 (-11)	0.67	0.1212	1.8 (-10)	0.68	1.6 (-10)

The position of the variational transition states, s^{VTST}, varies systematically from -0.01 to +0.10 a_0 for the folded saddle point as temperature increases from 200 K to 2000 K. Similarly, for the extended saddle point, s^{VTST} varies from -0.02 to +0.12 a_0 (over the same temperature range). We encountered a perplexing problem at large negative values of s. As depicted in **Figure 8**, there appear two maxima on the Gibbs free energy curve ($G^{\dagger}_{max}$): at +0.05 and -0.11 a_0. Additionally, the $G^{\dagger}_{max}$ at –0.11 a_0 did not arise from SCF energy and enthalpy, but perhaps from the entropy terms, and in turn from the behavior of the vibrational modes along the reaction path. **Table 6** lists the harmonic frequencies of the four lowest vibrational modes along the MEP. The frequency of the lowest-frequency mode changed from real to imaginary at approximately -0.07 a_0. At s < -0.07 a_0, this vibrational mode does not contribute to the entropy terms, and thereby gives rise to the $G^{\dagger}_{max}$ at -0.11 a_0. Similar behaviors have been reported for the analogous •OH + C_2H_6 reaction. As discussed by Hu et al.[51] and Natanson et al.,[52] low frequency modes computed along the MEP from the saddle point may at times become imaginary due to severely intermixed translational and rotational motion in the Cartesian coordinates. We have, however, decided to ignore the effect of $G^{\dagger}_{max}$ at -0.11 a_0 and only considered the variational rate constants determined near the saddle point. The variational corrections to the canonical rate constants were modest (< 10%) for both conformers at tropospherically relevant temperatures.

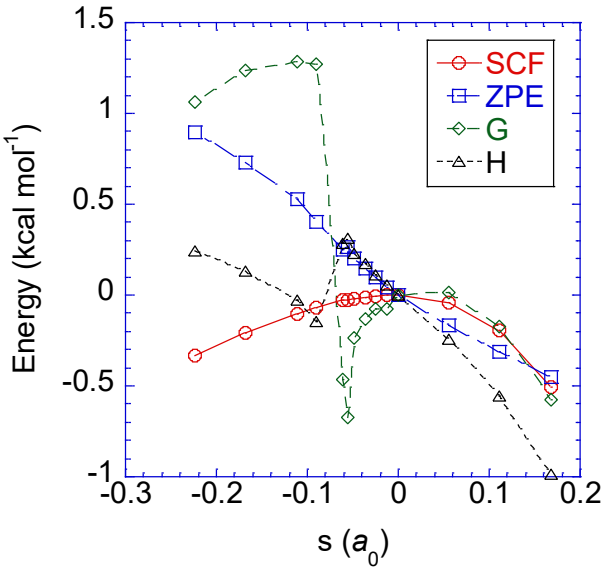

Figure 8. SCF energies without ZPE (SCF, red circle), ZPE (blue square), Gibbs free energies (G, green diamond), and enthalpy (H, black triangle) along the MEP relative to those at the saddle point (s = 0) for the BrHgO• + C_2H_6 reaction at M06-2X/AVTZ (298 K). We only display the folded conformer of the saddle point here, but the problem of low-lying and imaginary frequencies exists for both conformers.

Table 6. Harmonic frequencies of the four lowest vibrational modes along the MEP for the BrHgO• + C_2H_6 reaction at M06-2X/AVTZ.

s (a_0)	$\tilde{\nu}_i$ (cm^{-1})	$\tilde{\nu}$ (cm^{-1})	$\tilde{\nu}_2$ (cm^{-1})	$\tilde{\nu}_3$ (cm^{-1})
-0.1674	531.451*i*	42.052*i*	40.608	100.403
-0.1115	623.203*i*	28.694*i*	43.036	103.157
-0.0895	669.067*i*	21.209*i*	44.130	104.221
-0.0606	748.209*i*	8.448	45.502	105.719
-0.0559	771.181*i*	12.694	46.064	106.067
0.0000	997.392*i*	33.297	49.706	108.868

BrHgO• + NO/NO_2 reactions. Figure 9 displays the potential energy profiles for the BrHgO• + NO and BrHgO• + NO_2 reactions along with the results adapted from Jiao and Dibble.[15] For the barrierless addition to NO, BrHgO• reforms the O–N bond of 54.1 kcal mol^{-1} and produces its precursor BrHgONO, in either *anti* or *syn* conformer. Due to its stability however, *syn*-BrHgONO is most relevant regarding subsequent chemistry. The previous study has presented its structure and vibrational frequencies of BrHgONO at multiple levels of theory.[15] As a result, they are not discussed in the present work.

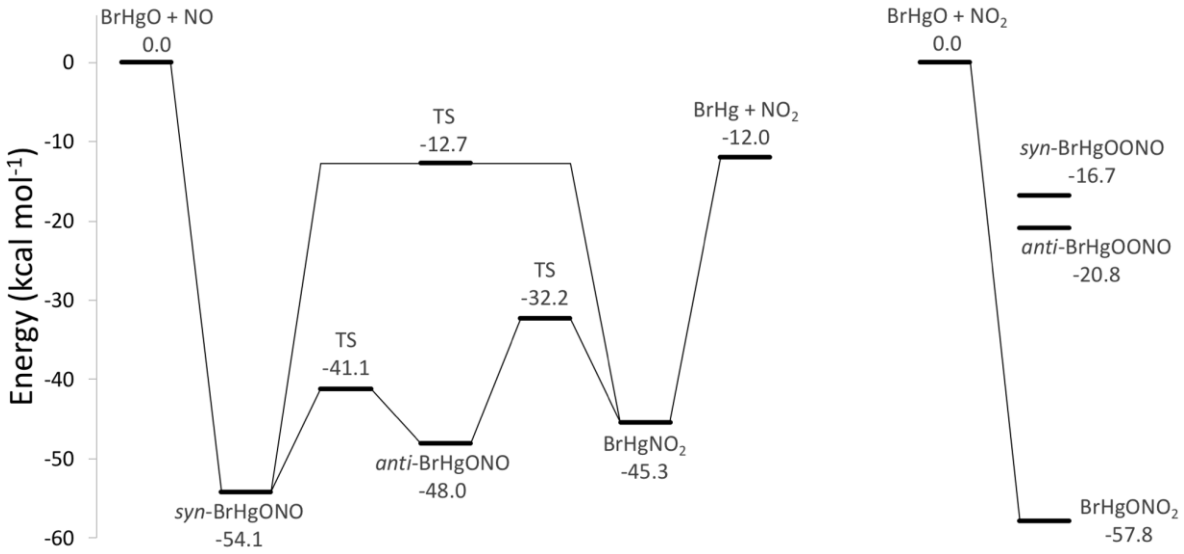

Figure 9. ZPE-corrected MEP for the BrHgO• + NO reaction along with the results adapted from Jiao and Dibble[15] at CCSD(T)//PBE0/AVTZ and the BrHgO• + NO_2 reaction at M06-2X/AVTZ.

Figure 10 displays the structures of all isomers in the BrHgO• + NO_2 system and **Table 7** lists the vibrational frequencies and IR intensities of $BrHgONO_2$. BrHgO• reacts with NO_2 to form $BrHgONO_2$ with a reaction enthalpy of 57.8 kcal mol^{-1} (at M06-2X/AVTZ). There exist two additional peroxynitrite conformers of the product: *syn*-BrHgOONO and *anti*-BrHgOONO, both of which lie approximately 30 kcal mol^{-1} above the nitrate form (i.e. $BrHgONO_2$). The *syn*, *anti*, and nitrate isomers in the BrHgO• + NO_2 system are analogous to the *cis-cis*, *trans-perp*, and nitrate forms in the •OH + NO_2[53] and RO• + NO_2[54] system, respectively. For simplicity, we refer to the *cis-cis* and *trans-perp* conformers of HOONO and ROONO as *cis-* and *trans-* instead. Their relative energies to each other are also qualitatively comparable to their counterparts, in that the nitrate forms (i.e., $BrHgONO_2$, $HONO_2$, and $RONO_2$) are the most stable (approximately -50 kcal mol^{-1} from reactants), whereas the *syn/cis* and *anti/trans* isomers are less stable but closer to each other (approximately -20 and -16 kcal mol^{-1} from reactants). By analogy to HOONO and ROONO, *syn-* and *anti*-BrHgOONO are expected to either decompose or isomerize to the stable nitrate. There exist few structural differences between the BrHgOONO conformers and their counterparts: *anti*-BrHgOONO has a planar symmetry but *syn*-BrHgOONO does not, whereas in the •OH system, *cis*-HOONO has a planar symmetry, but the *trans* conformer does not.[53] Note that, based on literature thermodynamics,[12,20] the production of BrHgOO• + NO from BrHgO• + NO_2 is endothermic by ~15 kcal mol^{-1}, suggesting that this product set can be neglected.

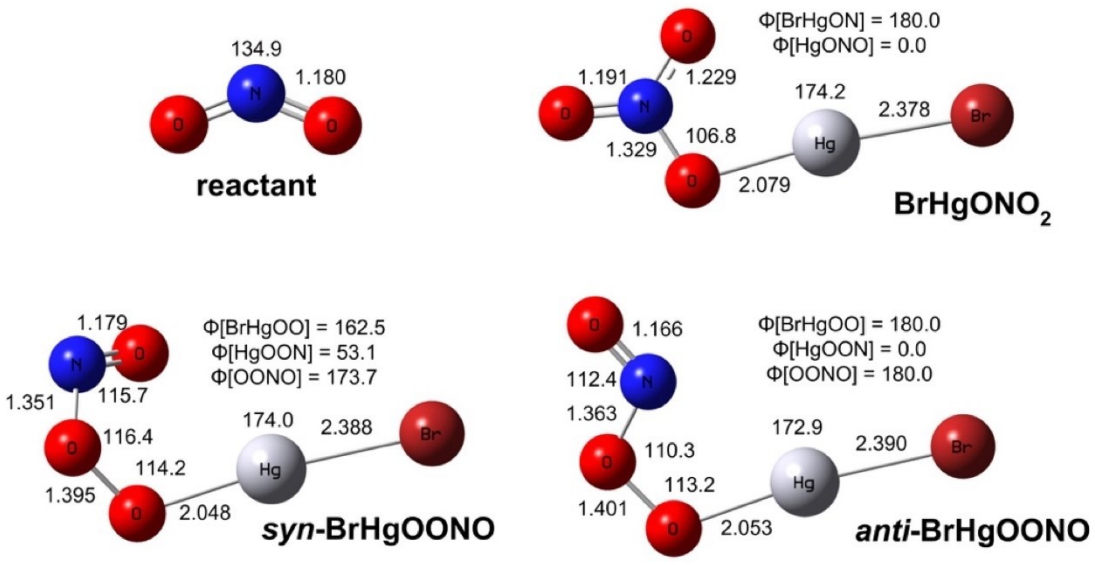

Figure 10. Reactants and all isomers of the product of the BrHgO• + NO_2 reaction at M06-2X/AVTZ. $BrHgONO_2$ and *anti*-BrHgOONO display C_s symmetry, whereas *syn*-BrHgOONO possesses C_1 symmetry. Distances are listed in Å and angles in degrees.

Table 7. Vibrational modes, symmetries, harmonic frequencies ($\tilde{\nu}$, in cm^{-1}), and integrated absorption intensities (S, in km mol^{-1}) of $BrHgONO_2$ at M06-2X/AVTZ.

Mode description	Symmetry	$\tilde{\nu}$	S
BrHgO in-plane bend	A'	62.0	2.71
BrHgO out-of-plane bend	A"	62.2	1.49
HgON in-plane bend	A'	145.3	7.57
HgON out-of-plane bend	A"	147.6	1.92
BrHg stretch	A'	247.5	2.58
HgO stretch	A'	344.5	51.7
NO_2 bend (scissoring)	A'	741.8	2.69
NO_2 bend (rocking)	A'	791.4	13.7
NO_3 out-of-plane bend	A"	846.5	11.9
NO stretch	A'	1035.5	356
NO_2 symmetric stretch	A'	1350.3	301
NO_2 asymmetric stretch	A'	1691.8	636

As mentioned in the Methods section, we decided not to compute the rate constants for the barrierless additions of NO and NO_2 to BrHgO• as part of the present work. In addition to the expensive cost of the computation, there exists no method to evaluate the accuracy of our rate constants. For the purpose of modeling BrHgO• chemistry, one may find it much more efficient, and perhaps no less accurate, to assume that their rate constants are equivalent to those of the analogous reactions CH_3O•

+ NO + M → CH_3ONO + M and CH_3O• + NO_2 + M → CH_3ONO_2 + M (2.9×10^{-11} and 1.7×10^{-11} molecules cm^{-3} s^{-1} at 298 K and 1 atm, respectively).[55]

ATMOSPHERIC IMPLICATIONS

Because BrHgO• can abstract hydrogen atoms from sp^3-hybridized carbon atoms (e.g., CH_4 and C_2H_6), one expects it to react with various VOCs in the atmosphere. Given a global average CH_4 concentration of 1.85 ppmv,[56] BrHgO• reacts with CH_4 with a pseudo-first order rate constant, k', of 10.5 s^{-1} at 298 K and 1 atm ($k' = k[CH_4]$ where k is the second-order rate constant). By contrast, abstraction from C_2H_6 proceeds with a slower pseudo-first order rate constant, varying from 0.02 s^{-1} up to only 0.3 s^{-1} at reasonable C_2H_6 concentrations of 0.2 ppbv and 3 ppbv,[56] respectively (at 298 K and 1 atm). Due to its high global tropospheric concentration, BrHgO• + CH_4 may dominate BrHgOH production via hydrogen abstraction from sp^3-hybridized carbons. Rate constants for the BrHgO• + CH_4 and BrHgO• + C_2H_6 at tropospheric temperatures (200 K ≤ T ≤ 333 K) can be fitted to the Arrhenius form as listed in **Table 8**.

Table 8. Arrhenius parameters (A in cm^3 $molecule^{-1}$ s^{-1} and E_a in kcal mol^{-1}) fitted to $k(T) = A \exp(-E_a/RT)$ for 200 K ≤ T ≤ 333 K. Rate constants are computed at CCSD(T)//M06-2X/AVTZ.

	$A/10^{-12}$	E_a
BrHgO• + CH_4 → BrHgOH + •CH_3	4.1	1.7
BrHgO• + C_2H_6 → BrHgOH + •C_2H_5	7.1	0.04

Table 9. Contribution of four trace gases to the fate of BrHgO•. Concentrations of CH_4 and C_2H_6 are adapted from global averages, and NO and NO_2 concentrations are seasonal averages from the 2016 New York City Community Air Survey (NYCCAS).[57]

	k (298 K, 1 atm) (cm^3 $molecule^{-1}$ s^{-1})	Concentration (summer, ppb)	Concentration (winter, ppb)	Summer (%)	Winter (%)
CH_4	2.3×10^{-13}	1850	1850	35	21
C_2H_6	6.5×10^{-12}	3	3	2	1
NO	2.9×10^{-11}	15	40	36	57
NO_2	1.7×10^{-11}	20	25	28	21

As global concentrations of NO and NO_2 average less than ~1 ppbv, it seems that the global fate of BrHgO• might be dominated by hydrogen abstraction to form BrHgOH. That being said, studies on the kinetics of BrHgO• reactions with unsaturated hydrocarbons and oxygenated VOCs are needed to verify this suggestion. By contrast, in urban areas, reactions of BrHgO• with NO and NO_2 may be competitive, as demonstrated here for New York City. **Table 9** lists the contributions of CH_4, C_2H_6, NO, and NO_2 to the fate of BrHgO• using NO and NO_2 seasonal averages from the 2016 New York City Community Air Survey (NYCCAS)[57] (at 298 K and 1 atm). Our result suggests the extent of NO addition to BrHgO• may be comparable to (in summertime) or prevail over (in wintertime) hydrogen abstraction from CH_4. Moreover, considering that our CCSD(T) barrier height for BrHgO• + CH_4 may underestimate the true value by ~1 kcal mol^{-1} (equivalent to a factor of 5 in the rate constant at 298 K), we expect a much lower contribution for CH_4 than presented here (down to 10% and 5% for

summer and winter, respectively). That being said, these estimates are limited by two assumptions in our analysis:

(1) Only those four trace gases contribute to the overall fate of BrHgO•: the assumption most likely fails due to other unexplored reactions of BrHgO• with other VOCs.
(2) Seasonal temperature changes have no effect on rate constants: as temperature decreases, rate constants of hydrogen abstractions from alkanes decrease, while those of additions to NO and NO_2 increase. That being said, the temperature dependencies of these rate constants are not strong: assuming temperature of 275 K (for wintertime), the contributions remain mostly the same, however (15%, 1%, 60%, 24% for CH_4, C_2H_6, NO, and NO_2, respectively).

Regarding the fates of thermally stable products, BrHgOH may subsequently undergo wet and dry deposition, assuming that, similar to other GOM species, it has low equilibrium vapor pressure and significant aqueous solubility. For the same reason, one may reasonably expect $BrHgONO_2$ to undergo wet and dry deposition, similar to $HONO_2$ and other studied GOM species. The photolysis lifetime of BrHgOH was computed to be ~1 day by Saiz-Lopez et al.[17] However, this lifetime seems fast, considering that $HgBr_2$, with which BrHgOH shares the same major chromophore, has a lifetime of 12 days. It should be noted, again, that Saiz-Lopez et al. assumed *syn*-BrHgONO photolysis to dissociate to BrHg• or Hg(0), which seems inconstant with our findings for the S_1 state. **Figure 11** displays the overall mechanism of the Hg(0) oxidation initiated by Br•, including the photolysis of BrHgONO and the subsequent BrHgO• chemistry. The overall atmospheric fate of BrHgO• may not yet be evaluated without considering other possible reactions—including reactions with oxygenated VOCs and unsaturated hydrocarbons. Investigations on reactions of BrHgO• with alkenes, carbonyls, and aromatics are critically needed to understand the fate of BrHgO• and the identity of Hg(II) compounds initially formed in the atmosphere.

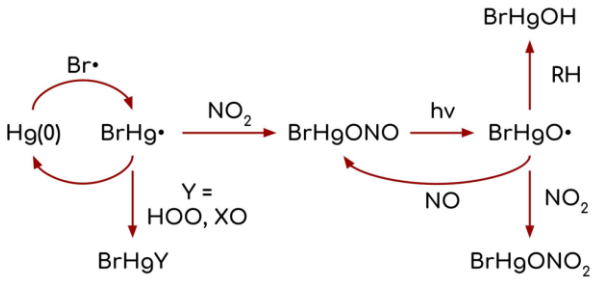

Figure 11. Mechanism of the GEM oxidation initiated by Br•, including the photolysis of *syn*-BrHgONO and the subsequent BrHgO• chemistry.

SUPPORTING INFORMATION

Tables of absolute energies, ZPEs, Cartesian coordinates, vibrational frequencies, and rotational constants for all species are available in the Supporting Information. In addition, Tables of SCF energies and Gibbs free energy as a function of temperature along the MEPs for the BrHgO• + CH_4 and BrHgO• + C_2H_6 reactions are included.

AUTHOR INFORMATION

*Corresponding author: tsdibble@esf.edu

ACKNOWLEDGEMENTS

We thank the National Science Foundation for their support of the present work under award number 1609848. The project used computing resources at Extreme Science and Engineering Discovery Environment (XSEDE), supported by the National Science Foundation grant number ACI-1053575; in particular, we used the Comet cluster at the San Diego Supercomputing Center (SDSC) and the Bridges system at the Pittsburgh Supercomputing Center (PSC).

REFERENCES

(1) Driscoll, C. T.; Mason, R. P.; Chan, H. M.; Jacob, D. J.; Pirrone, N. Mercury as a Global Pollutant: Sources, Pathways, and Effects. *Environ. Sci. Technol.* **2013**, *47* (10), 4967–4983.

(2) Holmes, C. D.; Jacob, D. J.; Corbitt, E. S.; Mao, J.; Yang, X.; Talbot, R.; Slemr, F. Global Atmospheric Model for Mercury Including Oxidation by Bromine Atoms. *Atmos. Chem. Phys.* **2010**, *10* (24), 12037–12057.

(3) Lin, C.-J.; Pongprueksa, P.; Lindberg, S. E.; Pehkonen, S. O.; Byun, D.; Jang, C. Scientific Uncertainties in Atmospheric Mercury Models I: Model Science Evaluation. *Atmos. Environ.* **2006**, *40* (16), 2911–2928.

(4) Lin, C.-J.; Pongprueksa, P.; Russell Bullock, O.; Lindberg, S. E.; Pehkonen, S. O.; Jang, C.; Braverman, T.; Ho, T. C. Scientific Uncertainties in Atmospheric Mercury Models II: Sensitivity Analysis in the CONUS Domain. *Atmos. Environ.* **2007**, *41* (31), 6544–6560.

(5) Wang, S.; Schmidt, J. A.; Baidar, S.; Coburn, S.; Dix, B.; Koenig, T. K.; Apel, E.; Bowdalo, D.; Campos, T. L.; Eloranta, E.; et al. Active and Widespread Halogen Chemistry in the Tropical and Subtropical Free Troposphere. *Proc. Natl. Acad. Sci. U. S. A.* **2015**, *112* (30), 9281–9286.

(6) Custard, K. D.; Thompson, C. R.; Pratt, K. A.; Shepson, P. B.; Liao, J.; Huey, L. G.; Orlando, J. J.; Weinheimer, A. J.; Apel, E.; Hall, S. R.; et al. The NO_x Dependence of Bromine Chemistry in the Arctic Atmospheric Boundary Layer. *Atmos. Chem. Phys.* **2015**, *15* (18), 10799–10809.

(7) Horowitz, H. M.; Jacob, D. J.; Zhang, Y.; Dibble, T. S.; Slemr, F.; Amos, H. M.; Schmidt, J. A.; Corbitt, E. S.; Marais, E. A.; Sunderland, E. M. A New Mechanism for Atmospheric Mercury Redox Chemistry: Implications for the Global Mercury Budget. *Atmos. Chem. Phys* **2017**, *17*, 6353–6371.

(8) Holmes, C. D.; Jacob, D. J.; Yang, X. Global Lifetime of Elemental Mercury against Oxidation by Atomic Bromine in the Free Troposphere. *Geophys. Res. Lett.* **2006**, *33* (20), L20808.

(9) Ariya, P. A.; Khalizov, A.; Gidas, A. Reactions of Gaseous Mercury with Atomic and Molecular Halogens: Kinetics, Product Studies, and Atmospheric Implications. *J. Phys. Chem. A* **2002**, *106* (32), 7310–7320.

(10) Goodsite, M. E.; Plane, J. M. C.; Skov, H. A Theoretical Study of the Oxidation of Hg^0 to $HgBr_2$ in the Troposphere. *Environ. Sci. Technol.* **2004**, *38* (6), 1772–1776.

(11) Shepler, B. C.; Balabanov, N. B.; Peterson, K. A. Hg + Br → HgBr Recombination and Collision-Induced Dissociation Dynamics. *J. Chem. Phys.* **2007**, *127* (16), 164304.

(12) Shepler, B. C.; Balabanov, N. B.; Peterson, K. A. Ab Initio Thermochemistry Involving Heavy Atoms: An Investigation of the Reactions Hg + IX (X = I, Br, Cl, O). *J. Phys. Chem. A* **2005**, *109* (45), 10363–10372.

(13) Dibble, T. S.; Zelie, M. J.; Mao, H. Thermodynamics of Reactions of ClHg and BrHg Radicals with Atmospherically Abundant Free Radicals. *Atmos. Chem. Phys. Chem. Phys. Discuss* **2012**, *12* (21), 10271–10279.

(14) Coburn, S.; Dix, B.; Edgerton, E.; Holmes, C. D.; Kinnison, D.; Liang, Q.; ter Schure, A.; Wang, S.; Volkamer, R. Mercury Oxidation from Bromine Chemistry in the Free Troposphere over the Southeastern US. *Atmos. Chem. Phys.* **2016**, *16* (6), 3743–3760.

(15) Jiao, Y.; Dibble, T. S. First Kinetic Study of the Atmospherically Important Reactions BrHg• + NO_2 and BrHg• + HOO. *Phys. Chem. Chem. Phys.* **2017**, *19* (3), 1826–1838.

(16) Ye, Z.; Mao, H.; Driscoll, C. T.; Wang, Y.; Zhang, Y.; Jaeglé, L. Evaluation of CMAQ Coupled with a State-of-the-Art Mercury Chemical Mechanism (CMAQ-NewHg-Br). *J. Adv. Model. Earth Syst.* **2018**, *10* (3), 668–690.

(17) Saiz-Lopez, A.; Sitkiewicz, S. P.; Roca-Sanjuán, D.; Oliva-Enrich, J. M.; Dávalos, J. Z.; Notario, R.; Jiskra, M.; Xu, Y.; Wang, F.; Thackray, C. P.; et al. Photoreduction of Gaseous Oxidized Mercury Changes Global Atmospheric Mercury Speciation, Transport and Deposition. *Nat. Commun.* **2018**, *9* (1), 4796–4805.

(18) Baker, H. J.; Seddon, N. Transient Absorption Processes in a Mercury Bromide Laser Discharge. *J. Phys. D. Appl. Phys.* **1988**, *21* (9), 1347–1351.

(19) Erlandson, A. C.; Cool, T. A. On the Regeneration Mechanism of $HgBr/_2$ in $HgBr/HgBr_2$ Dissociation Lasers. *Chem. Phys. Lett.* **1983**, *96* (6), 685–689.

(20) Balabanov, N. B.; Peterson, K. A. Mercury and Reactive Halogens: The Thermochemistry of Hg + {Cl_2 , Br_2 , BrCl, ClO, and BrO}. *J. Phys. Chem. A* **2003**, *107* (38), 7465–7470.

(21) Dunning, T. H. Gaussian Basis Sets for Use in Correlated Molecular Calculations. I. The Atoms Boron through Neon and Hydrogen. *J. Chem. Phys.* **1989**, *90* (2), 1007–1023.

(22) Kendall, R. A.; Dunning, T. H.; Harrison, R. J. Electron Affinities of the First-row Atoms Revisited. Systematic Basis Sets and Wave Functions. *J. Chem. Phys.* **1992**, *96* (9), 6796–6806.

(23) Peterson, K. A.; Shepler, B. C.; Figgen, D.; Stoll, H. On the Spectroscopic and Thermochemical Properties of ClO, BrO, IO, and Their Anions. *J. Phys. Chem. A* **2006**, *110* (51), 13877–13883.

(24) Peterson, K. A.; Puzzarini, C. Systematically Convergent Basis Sets for Transition Metals. II. Pseudopotential-Based Correlation Consistent Basis Sets for the Group 11 (Cu, Ag, Au) and 12 (Zn, Cd, Hg) Elements. *Theor. Chem. Acc.* **2005**, *114* (4–5), 283–296.

(25) Sitkiewicz, S. P.; Oliva, J. M.; Dávalos, J. Z.; Notario, R.; Saiz–Lopez, A.; Alcoba, D. R.; Oña, O. B.; Roca-Sanjuán, D. *Ab Initio* Quantum–Chemical Computations of the Electronic States in $HgBr_2$ and IBr: Molecules of Interest on the Earth's Atmosphere. *J. Chem. Phys.* **2016**, *145* (24), 244304.

(26) Bauernschmitt, R.; Ahlrichs, R. Treatment of Electronic Excitations within the Adiabatic Approximation of Time Dependent Density Functional Theory. *Chem. Phys. Lett.* **1996**, *256* (4–5), 454–464.

(27) Frisch, M. J.; Trucks, G. W.; Schlegel, H. B.; Scuseria, G. E.; Robb, M. A.; Cheeseman, J. R.; Scalmani, G.; Barone, V.; Petersson, G. A.; Nakatsuji, H.; et al. Gaussian 09, Revision D.01. Gaussian, Inc.: Wallingford, CT 2016.

(28) Stanton, J. F.; Bartlett, R. J. The Equation of Motion Coupled-cluster Method. A Systematic

Biorthogonal Approach to Molecular Excitation Energies, Transition Probabilities, and Excited State Properties. *J. Chem. Phys.* **1993**, *98* (9), 7029–7039.

(29) Scuseria, G. E.; Janssen, C. L.; Schaefer, H. F. An Efficient Reformulation of the Closed-shell Coupled Cluster Single and Double Excitation (CCSD) Equations. *J. Chem. Phys.* **1988**, *89* (12), 7382–7387.

(30) Stanton, J. F.; Gauss, J.; Cheng, L.; Harding, M. E.; Matthews, D. A.; Szalay, P. G. CFOUR, Coupled-Cluster Techniques for Computational Chemistry, a Quantum-Chemical Program Package.

(31) Adamo, C.; Barone, V. Toward Reliable Density Functional Methods without Adjustable Parameters: The PBE0 Model. *J. Chem. Phys.* **1999**, *110* (13), 6158.

(32) Zhao, Y.; Truhlar, D. G. The M06 Suite of Density Functionals for Main Group Thermochemistry, Thermochemical Kinetics, Noncovalent Interactions, Excited States, and Transition Elements: Two New Functionals and Systematic Testing of Four M06-Class Functionals and 12 Other Function. *Theor. Chem. Acc.* **2008**, *120* (1–3), 215–241.

(33) Raghavachari, K.; Trucks, G. W.; Pople, J. A.; Head-Gordon, M. A Fifth-Order Perturbation Comparison of Electron Correlation Theories. *Chem. Phys. Lett.* **1989**, *157* (6), 479–483.

(34) Gratien, A.; Lefort, M.; Picquet-Varrault, B.; Orphal, J.; Doussin, J.-F.; Flaud, J.-M. Experimental Intercomparison of the Absorption Cross-Sections of Nitrous Acid (HONO) in the Ultraviolet and Mid-Infrared Spectral Regions. *J. Quant. Spectrosc. Radiat. Transf.* **2009**, *110* (4–5), 256–263.

(35) Johnston, H. S.; Graham, R. Photochemistry of NO_x and HNO_x Compounds. *Can. J. Chem.* **1974**, *52* (8), 1415–1423.

(36) Shan, J. H.; Vorsa, V.; Wategaonkar, S. J.; Vasudev, R. Influence of Intramolecular Vibrational Dynamics on State-to-state Photodissociation: *Trans* DONO (A˜) versus HONO (A˜). *J. Chem. Phys.* **1989**, *90* (10), 5493–5500.

(37) Cotting, R.; Huber, J. R. Predissociation of HONO upon Excitation into the S1 State: An Ab Initio and Dynamics Study. *J. Chem. Phys.* **1996**, *104* (16), 6208.

(38) Schinke, R.; Untch, A.; Suter, H. U.; Huber, J. R. Mapping of Transition-state Wave Functions: I. Rotational State Distributions Following the Decay of Long-lived Resonances in the Photodissociation of HONO (S_1). *J. Chem. Phys.* **1991**, *94* (12), 7929–7936.

(39) Nonella, M.; Huber, J. R.; Untch, A.; Schinke, R. Photodissociation of CH_3ONO in the First Absorption Band: A Three-dimensional Classical Trajectory Study. *J. Chem. Phys.* **1989**, *91* (1), 194–204.

(40) Yu, S.-Y.; Zhang, C.-G.; Huang, M.-B. Electronic States of the *Cis*- and *Trans*-CH_3ONO Molecules: A CASPT2 Study. *Mol. Phys.* **2007**, *105* (23–24), 2977–2986.

(41) Amarasinghe, C.; Kamasah, A.; Foley, C. D.; Thompson, J. O. F.; Suits, A. G. Imaging the Photodissociation Dynamics of Nitrous Acid (HONO): The Role of Torsion. *J. Phys. Chem. A* **2017**, *121* (40), 7503–7510.

(42) Reisler, H.; Noble, M.; Wittig, C. Photodissociation of Aliphatic Nitrites – RONO. In

Molecular Photodissociation Dynamics (Advances in Gas-Phase Photochemistry and Kinetics); Ashford, M. N. R., Baggott, J. E., Eds.; The Royal Society of Chemistry: London, 1987; pp 162–176.

(43) Atkinson, R.; Arey, J. Atmospheric Degradation of Volatile Organic Compounds. *Chem. Rev.* **2003**, *103* (12), 4605–4638.

(44) Montero-Campillo, M. M.; Lamsabhi, A. M.; Mó, O.; Yáñez, M. Alkyl Mercury Compounds: An Assessment of DFT Methods. *Theor. Chem. Acc.* **2013**, *132* (3), 1328.

(45) Jiao, Y.; Dibble, T. S. Quality Structures, Vibrational Frequencies, and Thermochemistry of the Products of Reaction of BrHg• with NO_2 , HO_2 , ClO, BrO, and IO. *J. Phys. Chem. A* **2015**, *119* (42), 10502–10510.

(46) Ellingson, B. A.; Pu, J.; Lin, H.; Zhao, Y.; Truhlar, D. G. Multicoefficient Gaussian-3 Calculation of the Rate Constant for the OH + CH_4 Reaction and Its $^{12}C/^{13}C$ Kinetic Isotope Effect with Emphasis on the Effects of Coordinate System and Torsional Treatment. *J. Phys. Chem. A* **2007**, *111* (45), 11706–11717.

(47) Hashimoto, T.; Iwata, S. Theoretical Study on the Weakly-Bound Complexes in the Reactions of Hydroxyl Radical with Saturated Hydrocarbons (Methane, Ethane, and Propane). *J. Phys. Chem. A* **2002**, *106* (11), 2652–2658.

(48) Clarke, J. H. R.; Woodward, L. A. Raman Spectra of Monohalide Complexes of Mercury (II) in Aqueous Solution. *Trans. Faraday Soc.* **1965**, *61*, 207–211.

(49) Li, J.; Guo, H. Thermal Rate Coefficients and Kinetic Isotope Effects for the Reaction OH + $CH_4 \rightarrow H_2O + CH_3$ on an Ab Initio-Based Potential Energy Surface. *J. Phys. Chem. A* **2018**, *122* (10), 2645–2652.

(50) Melissas, V. S.; Truhlar, D. G. Interpolated Variational Transition State Theory and Tunneling Calculations of the Rate Constant of the Reaction OH + CH_4 at 223–2400 K. *J. Chem. Phys.* **1993**, *99* (2), 1013–1027.

(51) Hu, W.-P.; Liu, Y.-P.; Truhlar, D. G. Variational Transition-State Theory and Semiclassical Tunnelling Calculations with Interpolated Corrections: A New Approach to Interfacing Electronic Structure Theory and Dynamics for Organic Reactions. *J. Chem. Soc. Faraday Trans.* **1994**, *90* (12), 1715–1725.

(52) Natanson, G. A.; Garrett, B. C.; Truong, T. N.; Joseph, T.; Truhlar, D. G. The Definition of Reaction Coordinates for Reaction-Path Dynamics. *J. Chem. Phys.* **1991**, *94* (12), 7875–7892.

(53) Fry, J. L.; Nizkorodov, S. A.; Okumura, M.; Roehl, C. M.; Francisco, J. S.; Wennberg, P. O. *Cis-Cis* and *Trans-Perp* HOONO: Action Spectroscopy and Isomerization Kinetics. *J. Chem. Phys.* **2004**, *121* (3), 1432–1448.

(54) Launder, A. M.; Agarwal, J.; Schaefer, H. F. Exploring Mechanisms of a Tropospheric Archetype: CH_3O_2 + NO. *J. Chem. Phys.* **2015**, *143* (23), 234302.

(55) Burkholder, J. B.; Sander, S. P.; Abbatt, J.; Barker, J. R.; Huie, R. E.; Kolb, C. E.; Kurylo, M. J.; Orkin, V. L.; Wilmouth, M. D.; Wine, P. H. Chemical Kinetics and Photochemical Data for Use in Atmospheric Studies, Evaluation No. 18. JPL Publication 15-10, Jet Propulsion Laboratory, Pasadena. 2015.

(56) Blake., D. Methane, Nonmethane Hydrocarbons, Alkyl Nitrates, and Chlorinated Carbon Compounds Including 3 Chlorofluorocarbons (CFC-11, CFC-12, and CFC-113) in Whole-Air Samples. Carbon Dioxide Information Analysis Center, Oak Ridge National Laboratory, U.S. Department of Energy, Oak Ridge Tenn., U.S.A. 2013.

(57) NYC Community Air Survey (NYCCAS). New York City Department of Health and Mental Hygiene 2016.

TOC GRAPHIC